CAAP Quarterly Report

Date of Report: 06/29/2020

Prepared for: *U.S. DOT Pipeline and Hazardous Materials Safety Administration*

Contract Number: 693JK31950008CAAP

Project Title: Distributed Fiber Optic Sensor Network for Real-time Monitoring of Pipeline Interactive Anomalies

Prepared by: Dr. Yi Bao and Dr. Ying Huang

Contact Information: Email: yi.bao@stevens.edu, Phone: (201) 216-5223

For quarterly period ending: 06/29/2019

Business and Activity Section

(a) Contract Activity

Discussion about contract modifications or proposed modifications

None.

Discussion about materials purchased

None.

(b) Status Update of Past Quarter Activities

High level summary of the work performed for the reporting period.

In the second quarter, the university research team partially completed Tasks I, II, and IV of the above mentioned project, including experimental testing on the responses of two types of distributed fiber optic sensors subjected to deformations and corrosion, in addition to advising two graduate students and two undergraduate students, as well as an outreach event to primary school students in New Jersey on May 29th, 2020 to expand the educational impact of this project.

(c) Cost share activity

None.

(d) Task I: Developing and Characterizing Distributed Fiber Optic Sensors

In Task I, we aim to develop and characterize distributed fiber optic sensors under (i) deformation, (ii) corrosion, and (iii) excavation, as well as (iv) conducting a sensitivity study. In the third quarter, two activities were performed for Task I, including (1) developing a theoretical model to describe the responses of distributed fiber optic sensors subjected to deformations; (2) trainings of two graduate students and two undergraduate students for theoretical analysis of fiber optic sensors, and outreach activities with local primary school students including a virtual meeting with students and their teachers.

Detailed discussion and descriptions for the following:

1. Background

In the last quarterly report (the second report), distributed fiber optic sensors were experimentally tested under deformation and temperature changes. The sensitivity coefficients of the distributed fiber optic sensor were determined using the experimental data. However, it was unknown what are the fundamental mechanisms that control the responses of the distributed fiber optic sensors. In the PIs' previous research, it was found that point fiber optic sensor was subjected to the strain transfer effect [1], but there is lack of knowledge on the strain transfer effect in distributed fiber optic sensors [2]. Compared with point sensors, distributed fiber optic sensors are often subjected to nonuniform strain fields along the length of the sensors. In this study, the research team analyzed the strain transfer behavior and its effects on the measurement of deformations using the distributed fiber optic sensors.

2. Objectives

In the third quarterly research, there were three main objectives: (1) to quantitatively evaluate the strain transfer effect of distributed fiber optic sensors under uniform and nonuniform strain fields; (2) to experimentally test the analytical formulae for the distributed fiber optic sensors under strain changes; and (3) to characterize and calibrate the point fiber optic sensors.

3. Methodology

3.1. Literature review of strain transfer

Fiber optic sensors are usually packaged with protective coatings to enhance the mechanical strength and workability. Fig. 1 illustrates a representative telecommunication-grade, commercially available, single-mode optical fiber, which is known as a "bare" fiber because there is no additional protective packet. The optical fiber is composed of an 8.2-μm silica core and a 125-μm silica cladding. It is packaged with a dual-layer protective coating (Fig. 1) [2], including a 190-μm inner coating and a 242-μm outer coating. The inner coating is usually a soft, rubbery material that cushions the silica from external mechanical loads. The inner coating is surrounded by the outer coating, which is a much stiffer material that is used to protect the fiber from abrasions and environmental exposure. Both coatings are composed of complex mixtures of raw materials, such as monomers, oligomers, photoinitiators, and additives. The elastic moduli of the silica fiber (E_f), inner coating (E_i), and outer coating (E_o), are 72 GPa, 0.6 MPa, and 2 MPa, respectively. The Poisson's ratios of the fused silica fiber (μ_f), inner coating (μ_i), and outer coating (μ_o), are 0.26, 0.48, and 0.42, respectively. In real-life engineering practices, fiber optic cables with additional packages and reinforcement are often used. To develop the method for analyzing strain transfer effect, this study focuses on this type of fiber.

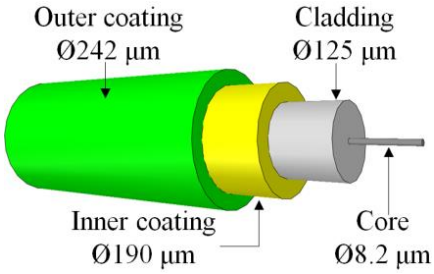

Fig. 1. Depiction of a single-model optical fiber packaged with a dual-layer polymer coating.

The sensors are either embedded in or attached on host materials for measurement. The strain changes sensed by fiber optic sensors can be different from (and usually smaller than) the strain changes in the host matrix because of the coating. This is known as the strain transfer effect.

Strain transfer effect has been extensively studied for point sensors in the literature [3-14]. For example, a theoretical study was conducted on the strain transfer of a coated fiber optic sensor embedded in a composite matrix based on the mechanics of elasticity [5]. The study assumed the host matrix to be infinite and subjected to a far-field longitudinal shear load parallel to both the optical and the structural fibers, and derived closed-form solutions for the strain transfer ratio based on the assumptions. It was found that the strain transfer was related to the coating thickness and the elastic moduli of the coating and host material [4]. The shear-lag theory was used to develop a mechanical model to describe the strain transfer behavior of a coated optical fiber embedded in a host matrix [3], and the model was validated using a white light Michelson interferometric sensor [6]. Subsequently, an expression of the axial strain distribution was derived for an embedded fiber optic sensor packaged with elastic coating material under an arbitrary strain field [8], and a theoretical strain transfer model was proposed to consider an ideal elastoplastic coating [9]. The strain transfer ratio was studied when the coating material worked at different stages (elastic, elastoplastic, plastic, and post-plastic) [11]. Based on the above advances, strain transfer behaviors have been considered for fiber Bragg grating (FBG) sensors under axial stresses [13] and non-axial stresses [12]. Furthermore, research was extended to multi-layer composite materials under a non-uniform strain field, and the FBG's reflection spectrum was observed to be broadened or even split into multiple peaks, which was different from a single sharp peak found in a uniform strain field [10]. Overall, the strain transfer ratio was about 0.90 to 0.96 and associated with the sensor's orientation [14]. In addition, it was found that the presence of packaged point sensors could affect the strain distribution in the host material [7].

The above review indicates that the previous studies focused on the strain transfer effect in point sensors, such as FBG and interferometer sensors. Due to the limited sensing length, most often, a point sensor can be considered working in uniform strain fields. In addition, the previous formulae for point sensors were validated in an average sense. The average strain transfer over the whole sensor length was derived and correlated to the strain measurements [6, 12]. However, this is not satisfied in distributed sensors, which are often used to measure non-uniform strain distributions [15, 16]. To date, the understanding of strain transfer in distributed sensors is still lacking, and there is no effective method to quantify the strain transfer effect in the case of distributed fiber optic sensors. Therefore, it remains a challenge to evaluate and improve the accuracy of strain measurement using distributed sensors.

3.2. Analytical study

This section derives the governing equations of strain transfer in a distributed fiber optic sensor embedded in a host structure, and solves the general and particular solutions under different representative boundary conditions of the host structure.

3.1.1. Governing equation

Fig. 2 illustrates an arbitrary infinitesimal segment of an optical fiber with a dual-layer coating embedded in host matrix. Typical types of host matrix include cementitious matrix (e.g., mortar or paste) and polymetric matrix (e.g., epoxy). The following assumptions are employed for the sake of simplicity: (1) All materials work linearly elastically. (2) All interfaces are well bonded. (3) Only stresses that are parallel to the optical fiber are considered. (4) The impact of the optical fiber's presence

on the host matrix's strain field is neglected. Due to symmetry, only a half structure is shown in Fig. 2. The shear stresses in the inner and outer coatings are represented by $\tau_i(x, r)$ and $\tau_o(x, r)$, respectively. The shear stress between the host matrix and the outer coating is represented by $\tau_o(x, r_o)$. The shear stress between the outer and inner coatings is represented by $\tau_i(x, r_i)$. The shear stress at the interface between the inner coating and the fiber core is represented by $\tau_f(x)$. The normal stresses in the fiber core, the outer coating, the inner coating, and the vicinity of host matrix are represented by $\sigma_f(x)$, $\sigma_o(x)$, $\sigma_i(x)$, and $\sigma_h(x)$, respectively. The deformations of the optical fiber, inner coating, outer coating, and the host matrix are represented by δ_f, δ_o, δ_i, and δ_h, respectively, at x with a segment of dx length. The shear strains in inner and outer coatings are represented by γ_i and γ_o, respectively. For each segment, no deformation is shown on the left side. The deformations in Fig. 2 represent the total deformation of both sides.

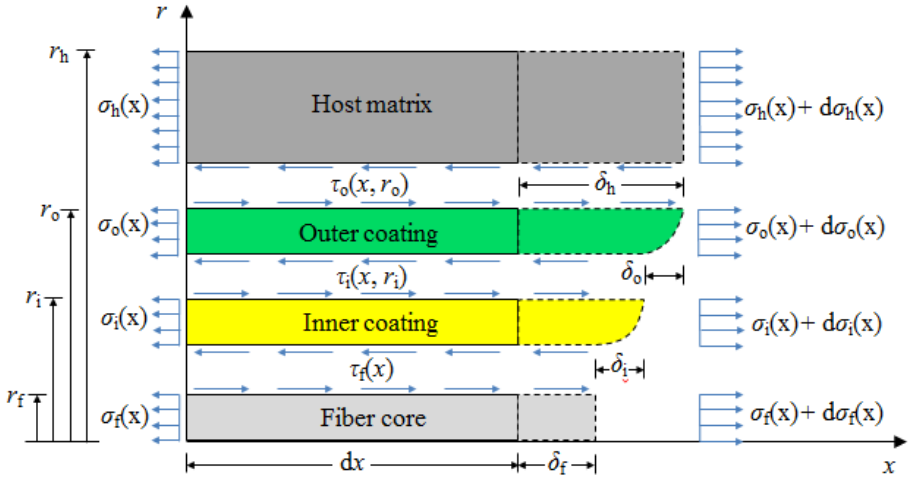

Fig. 2. Diagram for stress analysis of an optical fiber embedded in concrete.

Equations of equilibrium in the x-direction are:

$$(\pi r_f^2)\, d\,\sigma_f(x) + (2\pi r_f)\tau_f(x)\, d\,x = 0 \tag{1}$$

$$(\pi r^2 - \pi r_f^2)\, d\,\sigma_i\,(x) + (2\pi r_f)\tau_i(x,r)\, d\,x = (2\pi r_f)\tau_f(x)\, d\,x,\ r_f \le r \le r_i \tag{2}$$

$$(\pi r^2 - \pi r_i^2)\, d\,\sigma_o\,(x) + (2\pi r)\tau_o(x,r)\, d\,x = (2\pi r_i)\tau_i(x,r_i)\, d\,x,\ r_i \le r \le r_o \tag{3}$$

Considering that no force is directly applied on the coatings at $x = 0$, integrating from 0 to x, Eqs. (2) and (3) can be rewritten as:

$$(\frac{r^2-r_f^2}{2x})\sigma_i(x) + r\tau_i(x,r) = r_f\tau_f(x),\ r_f \le r \le r_i \tag{4}$$

$$(\frac{r^2-r_f^2}{2x})\sigma_o(x) + r\tau_o(x,r) = r_i\tau_i(x,r_i),\ r_i \le r \le r_o \tag{5}$$

Since the diameter of the optical fiber is small compared with its length, the first terms in Eqs. (4) and (5) vanish, except for the vicinity at the two ends of the optical fiber [6]. Then, Eqs. (4) and (5) can be rewritten as:

$$r\tau_i(x,r) = r_f\tau_f(x),\ r_f \le r \le r_i \tag{6}$$

$$r\tau_o(x,r) = r_i\tau_i(x,r_i) = r_f\tau_f(x),\ r_i \le r \le r_o \tag{7}$$

According to the assumption (1), the optical fiber's longitudinal strain can be expressed as:

$$\sigma_f(x) = E_f\varepsilon_f(x) \tag{8}$$

Thus, Eq. (1) can be rewritten as:

$$\tau_{\mathrm{f}}(x) = -\frac{E_{\mathrm{f}} r_{\mathrm{f}}}{2} \frac{d\,\varepsilon_{\mathrm{f}}(x)}{d\,x} \tag{9}$$

Plug Eq. (9) into Eqs. (6) and (7), respectively:

$$\tau_{\mathrm{i}}(x,r) = -\frac{E_{\mathrm{f}} r_{\mathrm{f}}^2}{2r} \frac{d\,\varepsilon_{\mathrm{f}}(x)}{d\,x},\ r_{\mathrm{f}} \le r \le r_{\mathrm{i}} \tag{10}$$

$$\tau_{o}(x,r) = -\frac{E_{\mathrm{f}} r_{\mathrm{f}}^2}{2r} \frac{d\,\varepsilon_{\mathrm{f}}(x)}{d\,x},\ r_{\mathrm{i}} \le r \le r_{\mathrm{o}} \tag{11}$$

According to the assumption (2), the deformations in Fig. 2 satisfy:

$$\delta_{\mathrm{h}} = \delta_{\mathrm{f}} + \delta_{\mathrm{i}} + \delta_{\mathrm{o}} \tag{12}$$

The longitudinal deformations of the host matrix and the glass fiber can be expressed as:

$$\delta_{\mathrm{h}} = \varepsilon_{\mathrm{h}}(x)\,\mathrm{d}\,x,\ \delta_{\mathrm{f}} = \varepsilon_{\mathrm{f}}(x)\,\mathrm{d}\,x \tag{13}$$

The strain transfer from the host matrix to the optical fiber core depends on the shear strain in the interlayer which is due to the relative deformation between the host matrix and fiber core. Therefore, for the inner and outer coatings:

$$\delta_{\mathrm{i}} = \int_{r_{\mathrm{f}}}^{r_{\mathrm{i}}} \mathrm{d}\,\gamma_{\mathrm{i}}\,(x,r)\,\mathrm{d}\,r = \frac{1}{G_{\mathrm{i}}} \int_{r_{\mathrm{f}}}^{r_{\mathrm{i}}} \mathrm{d}\,\tau_{\mathrm{i}}\,(x,r)\,\mathrm{d}\,r \tag{14}$$

$$\delta_{\mathrm{o}} = \int_{r_{\mathrm{i}}}^{r_{\mathrm{o}}} \mathrm{d}\,\gamma_{\mathrm{o}}\,(x,r)\,\mathrm{d}\,r = \frac{1}{G_{\mathrm{o}}} \int_{r_{\mathrm{i}}}^{r_{\mathrm{o}}} \mathrm{d}\,\tau_{\mathrm{o}}\,(x,r)\,\mathrm{d}\,r \tag{15}$$

where, $\gamma_{\mathrm{i}} = \tau_{\mathrm{i}} / G_{\mathrm{i}}$, and $\gamma_{\mathrm{o}} = \tau_{\mathrm{o}} / G_{\mathrm{o}}$.

Plug Eqs. (13), (14) and (15) into Eq. (12):

$$\varepsilon_{\mathrm{h}}(x)\mathrm{d}x = \varepsilon_{\mathrm{f}}(x)\,\mathrm{d}\,x + \frac{1}{G_{\mathrm{i}}} \int_{r_{\mathrm{f}}}^{r_{\mathrm{i}}} \mathrm{d}\,\tau_{\mathrm{i}}\,(x,r)\,\mathrm{d}\,r + \frac{1}{G_{\mathrm{o}}} \int_{r_{\mathrm{i}}}^{r_{\mathrm{o}}} \mathrm{d}\,\tau_{\mathrm{o}}\,(x,r)\,\mathrm{d}\,r \tag{16}$$

By substituting Eqs. (10) and (11) into Eq. (16), and rearranging the nonzero term dx, Eq. (16) can be rewritten as:

$$\varepsilon_{\mathrm{h}}(x) = \varepsilon_{\mathrm{f}}(x) - \frac{E_{\mathrm{f}} r_{\mathrm{f}}^2}{2} \left[\frac{\mathrm{In}(r_{\mathrm{i}}/r_{\mathrm{f}})}{G_{\mathrm{i}}} + \frac{\mathrm{In}(r_{\mathrm{o}}/r_{\mathrm{i}})}{G_{\mathrm{o}}} \right] \frac{d^2 \varepsilon_{\mathrm{f}}(x)}{\mathrm{d}x^2} \tag{17}$$

By introducing a positive coefficient k, Eq. (17) can be rewritten as:

$$\varepsilon_{\mathrm{f}}^{''}(x) - k^2 \varepsilon_{\mathrm{f}}(x) + k^2 \varepsilon_{\mathrm{h}}(x) = 0 \tag{18a}$$

$$k^2 = \frac{2}{E_{\mathrm{f}} r_{\mathrm{f}}^2 \left[\frac{\mathrm{In}(r_{\mathrm{i}}/r_{\mathrm{f}})}{G_{\mathrm{i}}} + \frac{\mathrm{In}(r_{\mathrm{o}}/r_{\mathrm{i}})}{G_{\mathrm{o}}} \right]} \tag{18b}$$

For the optical fiber packaged with a dual-layer coating (Fig. 1), k can be determined 55 m^{-1}, according to the optical fiber's dimensions and material properties.

The strain transfer in optical fibers with multi-layer coatings can be analyzed following the same process. As a matter of fact, Eq. (18b) can be extended to a generalized form for optical fibers with multi-layer coatings, as long as k^2 is modified as follows:

$$k^2 = \frac{2}{E_{\mathrm{f}} r_{\mathrm{f}}^2 [\frac{\mathrm{In}(r_1/r_{\mathrm{f}})}{G_1} + \frac{\mathrm{In}(r_2/r_1)}{G_2} + \cdots + \frac{\mathrm{In}(r_{\mathrm{n}}/r_{\mathrm{n}-1})}{G_{\mathrm{n}}}]} \tag{18c}$$

where n represents the number of coating layers.

3.1.2. Solutions

The solution of Eq. (18) can be expressed as [18]:

$$\varepsilon_{\mathrm{f}}(x) = C_1 \cosh(kx) + C_2 \sinh(kx) + \varepsilon^{\mathrm{p}}(x) \tag{19}$$

where the first two terms represent the general solution; the third term $\varepsilon^{\mathrm{p}}(x)$ is the particular solution associated with $\varepsilon_{\mathrm{h}}(x)$, which denotes the strain distribution in the host matrix along the optical fiber. The integration constants, C_1 and C_2, are determined by the boundary conditions.

In general, the form of $\varepsilon_{\mathrm{h}}(x)$ can be different in various problems. Thus, the particular solution $\varepsilon^{\mathrm{p}}(x)$ can be different, correspondingly. For an arbitrary condition, $\varepsilon_{\mathrm{h}}(x)$ can be expressed using a Fourier series. However, for a large amount of engineering problems, $\varepsilon_{\mathrm{h}}(x)$ can be segmentally expressed as or approximated by a series of polynomials, as shown in Eq. (20).

$$\varepsilon_{\mathrm{h}}(x) = \sum_{i=0}^{m} a_i x^i \tag{20}$$

where m represents the order, and a_i (i=0, 1, 2, … , m) represent the coefficients.

Correspondingly, $\varepsilon^{\mathrm{p}}(x)$ can be determined as a polynomial of the same order in each segment where $\varepsilon_{\mathrm{h}}(x)$ is continuous and differentiable regarding to x [18]. Therefore, $\varepsilon^{\mathrm{p}}(x)$ and $\varepsilon_{\mathrm{f}}(x)$ can be written as:

$$\varepsilon^{\mathrm{p}}(x) = \sum_{i=0}^{m} b_i x^i \tag{21a}$$

$$\varepsilon_{\mathrm{f}}(x) = C_1 \cosh(kx) + C_2 \sinh(kx) + \sum_{i=0}^{m} b_i x^i \tag{21b}$$

where b_i (i = 0, 1, 2, … , m) are the coefficients. The relationship between a_i and b_i are as follows.

When $m < 2$,

$$a_i = b_i \tag{22}$$

When $m \geq 2$,

$$a_i = \begin{cases} b_i & i = m-1, m \\ b_i - (i+2)(i+1)b_{i+2}/k^2 & i \leq m-2 \end{cases} \tag{23}$$

The strain transfer ratio is defined:

$$\alpha(x) = \varepsilon_{\mathrm{f}}(x)/\varepsilon_{\mathrm{h}}(x) \tag{24}$$

3.1.3. Uniform strain field

An optical fiber is attached along a pipe subjected to a uniform cross section, as shown in Fig. 3. The normal strain in the pipe is expressed as: $\varepsilon_{\mathrm{h}}(x) = \varepsilon_0$. The normal strain in the optical fiber can be determined from Eq. (21), as given in Eq. (25).

$$\varepsilon_{\mathrm{f}}(x) = C_1 \cosh(kx) + C_2 \sinh(kx) + \varepsilon_0 \tag{25}$$

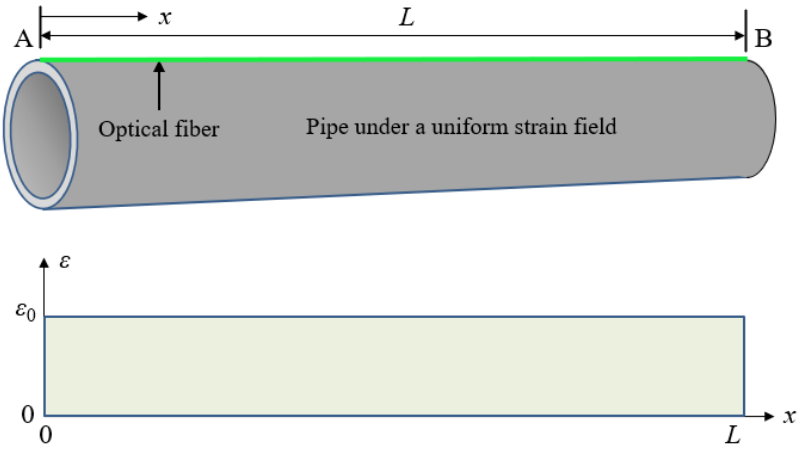

Fig. 3. Depiction of a pipe subjected to a uniform strain field. An optical fiber is attached on the pipe.

Then, the shear stress in the optical fiber can be determined from Eq. (10), as given in Eq. (26):

$$\tau_f(x) = -0.5\, E_f r_f [k C_1 \sinh(kx) + k C_2 \cosh(kx)] \quad (26)$$

The boundary conditions are:

$$\varepsilon_f(x = 0) = 0 \quad (27a)$$

$$\varepsilon_f(x = L) = 0 \quad (27b)$$

By substituting Eq. (27) into Eqs. (25) and (26), respectively, the coefficients C_1 and C_2 can be determined:

$$C_1 = -\varepsilon_0,\ C_2 = \varepsilon_0 \tanh(kL/2)$$

In this case, another boundary can be used to replace Eq. (27a) or Eq. (27b):

$$\tau_f(x = L/2) = 0 \quad (27c)$$

With Eq. (27c), the same results of the coefficients C_1 and C_2 can be obtained.

Therefore, the normal strain and shear stress are:

$$\varepsilon_f(x) = \varepsilon_0 [1 - \cosh(kx) + \tanh(kL/2) \sinh(kx)] \quad (28)$$

$$\tau_f(x) = -0.5 E_f r_f k \varepsilon_0 [\tanh(kL/2) \cosh(kx) - \sinh(kx)] \quad (29)$$

The strain transfer ratio is:

$$\alpha(x) = 1 - \cosh(kx) + \tanh(kL/2) \sinh(kx) \quad (30)$$

The strain transfer ratio can be plotted against x ($0 \le x \le L/2$ for the left half), as shown in Fig. 4(a). The right half ($L/2 < x \le L$) is symmetrical to the left half. At each end of the optical fiber, there is a development length where the measured strain is smaller than the real strain due to the strain transfer effect. The strain is gradually developed within that length, and the strain transfer ratio will be approximately 1.0 beyond that length. The development length is dependent on k that is related to the material and geometry of the optical fiber and independent of the applied strain ε_0. For the optical fiber with a dual-layer coating in this study, 95% of the strain could be developed in 55 mm, and 99% of strain could be developed in 84 mm. Eq. (30) can be used to correct the measured strains within the development length.

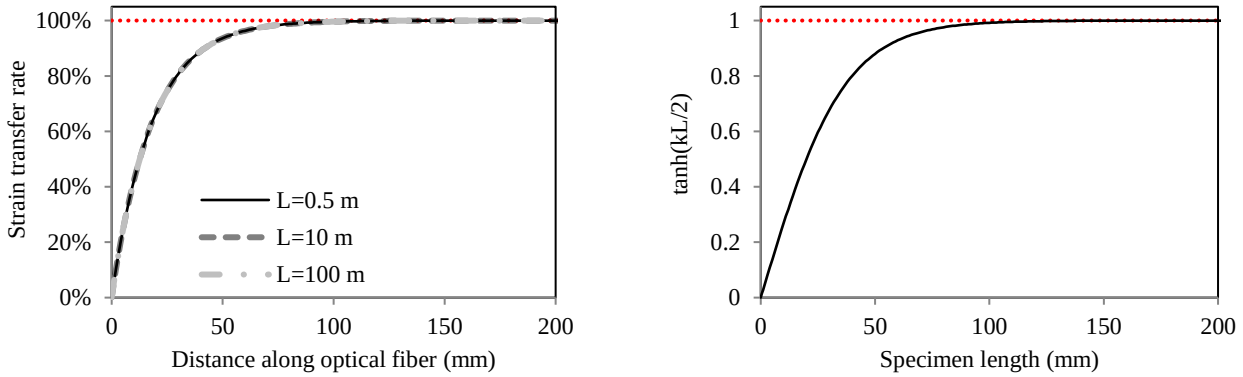

(a) (b)

Fig. 4. Strain transfer ratio in uniform strain field: (a) strain transfer ratio vs. distance; (b) tanh(kL/2) vs. specimen length.

As indicated in Eq. (30), the strain transfer ratio is dependent on L. With k = 55 m^{-1}, tanh(kL/2) increases to 0.95 at L = 66 mm, as shown in Fig. 4(b). When the specimen length is longer than 100 mm, the influence of specimen length will be negligible. Therefore, no significant difference can be observed between the three curves in Fig. 4(a).

3.1.4. Non-uniform strain field

A distributed fiber optic sensor can be subjected to a complex strain field, because of the long sensor length. In general, it might be difficult to use a single polynomial to describe the strain field, as illustrated in Fig. 5. Regarding an arbitrary strain field, the field can be divided into multiple segments along the length of the distributed fiber optic sensor. Within each segment, the strain field can be described using a single or combination of polynomials.

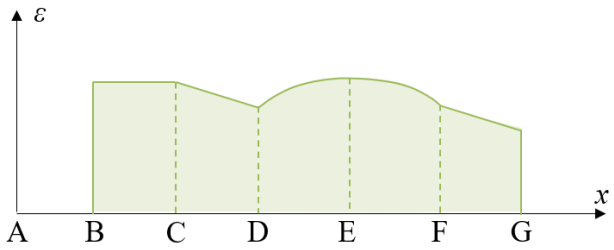

Fig. 5. Depiction of an arbitrary strain field of the host matrix. The strain field is divided into multiple segments along the length of the distributed fiber optic sensor.

Therefore, a general procedure for solving a non-uniform strain field is proposed: (1) Step 1: Judge whether the strain field needs to be divided into multiple segments, and determine the polynomial expression of the strain field. (2) Step 2: Determine the boundary conditions. If there are multiple segments, the boundary conditions of each segment should be determined. (3) Solve the strain distribution in the distributed fiber optic sensor. After the strain transfer within each segment is solved, the strain distribution along the entire fiber length can be obtained by combining all the segments.

A representative non-uniform strain field is investigated, as shown in Fig. 6. In the length (L) of the pipe between points A and B, the normal strain linearly increases from ε_1 to ε_2. Regarding pipes subjected to more complicated non-uniform strain fields, the pipe can be divided into multiple segments. When the length of the segments is small, each segment can be considered subjected to the representative strain field.

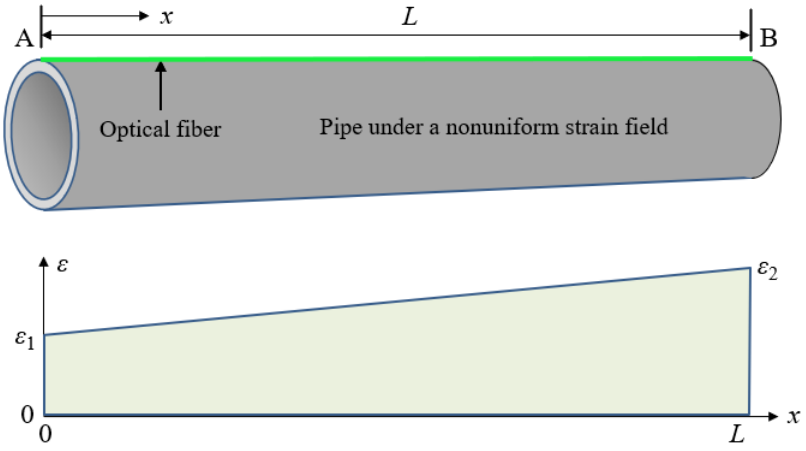

Fig. 6. Depiction of a pipe subjected to a non-uniform strain field. The strain distribution is linear along the length of the pipe.

To describe the relationship between ε_1 and ε_2, a factor λ is introduced:

$$\varepsilon_2 = \gamma\varepsilon_1 \tag{31}$$

The normal strain in the pipe can be expressed as:

$$\varepsilon_h(x) = \varepsilon_1 + \frac{(\varepsilon_2 - \varepsilon_1)x}{L} = \varepsilon_1[1 + \frac{(\gamma - 1)x}{L}] \quad (32)$$

Therefore, the normal strain and shear stress of the optical fiber are:

$$\varepsilon_f(x) = C_1 \cosh(kx) + C_2 \sinh(kx) + \varepsilon_1[1 + \frac{(\gamma - 1)x}{L}] \quad (33)$$

where C_1 and C_2 are the integration constants, which can be determined by the boundary conditions.

The boundary conditions are:

$$\varepsilon_f(x = 0) = 0 \quad (34a)$$

$$\varepsilon_f(x = L) = 0 \quad (34b)$$

The integration constants can be determined:

$$C_1 = -\varepsilon_1 \quad (35a)$$

$$C_2 = \gamma\varepsilon_1 \tanh(kL/2) \quad (35a)$$

The strain transfer ratio can be determined:

$$\alpha(x) = 1 - \frac{\gamma \tanh\left(\frac{kL}{2}\right)\sinh(kx) - \cosh(kx)}{1 + \frac{(\gamma - 1)x}{L}} \quad (36)$$

The strain in the distributed fiber optic sensor can be plotted against x/L, as shown in Fig. 7(a). The strain in the distributed fiber optic sensor is lower than the strain in the host matrix within the development lengths at the two ends of the distributed fiber optic sensor. Beyond the development length, the strain in the middle length of the distributed fiber optic sensor is the same as the strain in the host matrix. The strain transfer ratio along the length of the distributed fiber optic sensor is plotted in Fig. 7(b), consistent with the distribution of the strain transfer ratio shown in Fig. 4.

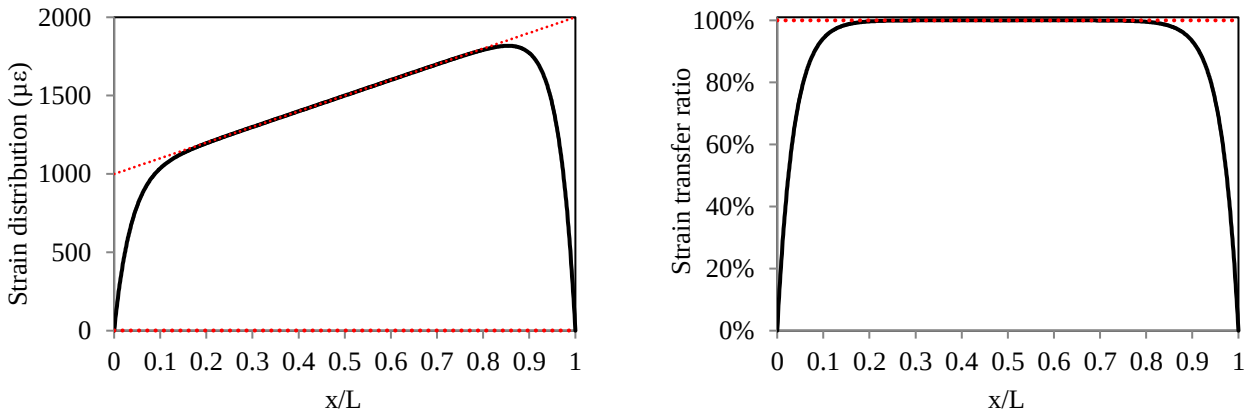

(a) (b)

Fig. 7. Strain transfer analysis results: (a) strain distribution in the distributed fiber optic sensor; and (b) strain transfer ratio along the length of the distributed fiber optic sensor.

Based on the above analysis on a single segment with non-uniform strain distribution, further analysis is performed for multiple segments with different non-uniform strain distributions, as depicted in Fig. 8. According to the strain distribution, the pipe is divided into two segments, designated as A-C and C-B, respectively. Within each segment, the strain linearly changes from one end to the other end of the segment. The lengths of the two segments are *a* and *b*, respectively, and the total length is denoted as *L* (*L* = *a* + *b*). Within the segment A-C, the strain changes from ε_1 to ε_0. Within the segment C-B, the strain changes from ε_0 to ε_2.

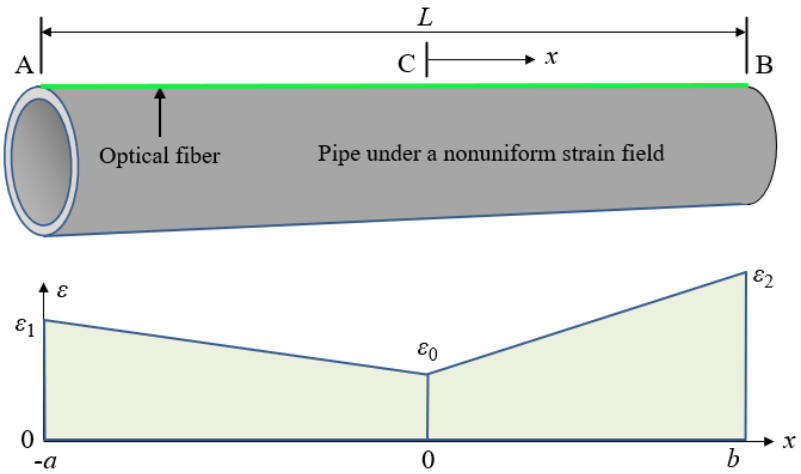

Fig. 8. Depiction of a pipe subjected to a non-uniform strain field. The entire length of the pipe is divided into two segments, and the strain distribution is linear along the length of each segment.

To describe the relationship between ε_0, ε_1 and ε_2, two factors (λ_1 and λ_2) are introduced:

$$\varepsilon_1 = \gamma_1 \varepsilon_0 \tag{37a}$$

$$\varepsilon_2 = \gamma_2 \varepsilon_0 \tag{37b}$$

The normal strain in the pipe can be expressed as:

$$\varepsilon_{\mathrm{h}}(x) = \begin{cases} \varepsilon_0[1 - \frac{(\gamma_1 - 1)x}{a}] & x < 0 \\ \varepsilon_0[1 + \frac{(\gamma_2 - 1)x}{b}] & x \geq 0 \end{cases} \tag{38}$$

Therefore, the normal strain of the optical fiber is expressed as:

$$\varepsilon_{\mathrm{f}}(x) = \begin{cases} C_1 \cosh(kx) + C_2 \sinh(kx) + \varepsilon_0[1 - \frac{(\gamma_1 - 1)x}{a}] & x < 0 \\ C_3 \cosh(kx) + C_4 \sinh(kx) + \varepsilon_0[1 + \frac{(\gamma_2 - 1)x}{b}] & x \geq 0 \end{cases} \tag{39}$$

where C_1 and C_2 are the integration constants, which can be determined by the boundary conditions.

The boundary conditions are:

$$\varepsilon_{\mathrm{f}}(x = -a) = 0 \tag{40a}$$

$$\varepsilon_{\mathrm{f}}(x = 0^-) = \varepsilon_{\mathrm{f}}(x = 0^+) \tag{40b}$$

$$\tau_{\mathrm{f}}(x = 0^-) = \tau_{\mathrm{f}}(x = 0^+) \tag{40c}$$

$$\varepsilon_{\mathrm{f}}(x = b) = 0 \tag{40d}$$

The integration constants can be determined:

$$C_1 = C_3 \tag{41a}$$

$$C_2 = C_4 + \varepsilon_0(\frac{\gamma_1 - 1}{ka} + \frac{\gamma_2 - 1}{kb}) \tag{41b}$$

$$C_3 = -\frac{C_4 \sinh(kb) + \gamma_2 \varepsilon_0}{\cosh(kb)} \tag{41c}$$

$$C_4 = \varepsilon_0 \frac{\gamma_1 \cosh(kb) - \gamma_2 \cosh(ka) - (\frac{\gamma_1 - 1}{ka} + \frac{\gamma_2 - 1}{kb}) \sinh(ka) \cosh(kb)}{\sinh(ka + kb)} \tag{41d}$$

The strain distribution in the distributed fiber optic sensor can be obtained by plugging Eq. (41) into Eq. (39).

The strain in the distributed fiber optic sensor can be plotted against x/L, as shown in Fig. 9(a). The

strain in the distributed fiber optic sensor is lower than the strain in the host matrix within the development lengths at the two ends of segment. Beyond the development length, the strain in the middle length of segment is the same as the strain in the host matrix. The strain transfer ratio along the length of the distributed fiber optic sensor is plotted in Fig. 9(b).

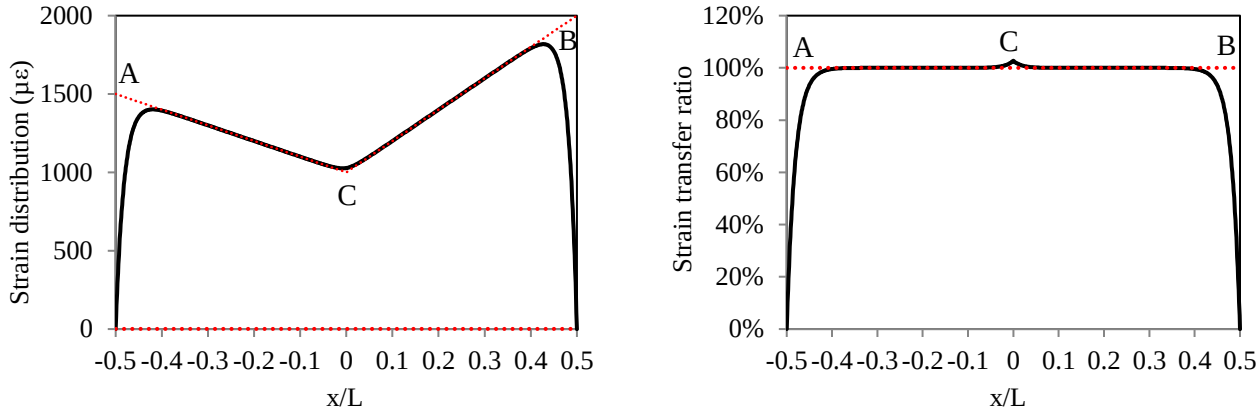

Fig. 9. Strain transfer analysis results: (a) strain distribution in the distributed fiber optic sensor; and (b) strain transfer ratio along the sensor length. In this figure, $a = b = 0.5$ m; $\gamma_1 = 1.5$, and $\gamma_2 = 2$.

The strain transfer ratio at $x = 0$ can be determined:

$$\alpha(x=0) = \frac{\varepsilon_f(x=0)}{\varepsilon_h(x=0)} = 1 - \frac{\gamma_1/\cosh(ka) - \gamma_2/\cosh(kb) - \left(\frac{\gamma_1-1}{ka} + \frac{\gamma_2-1}{kb}\right)\tanh(ka)}{\tanh(ka)/\tanh(kb)+1} - \frac{\gamma_2}{\cosh(kb)} \tag{42}$$

When a and b reach 0.096 m, the values of cosh(ka) and cosh(kb) reach 100; and the values of tanh(ka) and tanh(kb) are more than 0.9999. Thus, the strain transfer ratio at $x = 0$ can be rewritten as:

$$\alpha(x=0) \approx 1 - \frac{0 - 0 - \left(\frac{\gamma_1-1}{ka} + \frac{\gamma_2-1}{kb}\right)}{1+1} - 0 = 1 + \frac{\gamma_1-1}{2ka} + \frac{\gamma_2-1}{2kb} \tag{43}$$

When $a = b = L/2$, the strain transfer ratio at $x = 0$ can be rewritten as:

$$\alpha(x=0) \approx 1 + \frac{\gamma_1+\gamma_2-2}{kL} \tag{44}$$

The strain transfer ratio at x = 0 (point C in Fig. 9) is plotted in Fig. 10. Given k = 55 m-1 and L = 1.0 m, the strain transfer ratio at the interface between the two segments (A-C and C-B) follow a linear relationship with ($\gamma_1 + \gamma_2$). It is shown that Eq. (44) provides good estimations compared with Eq. (42).

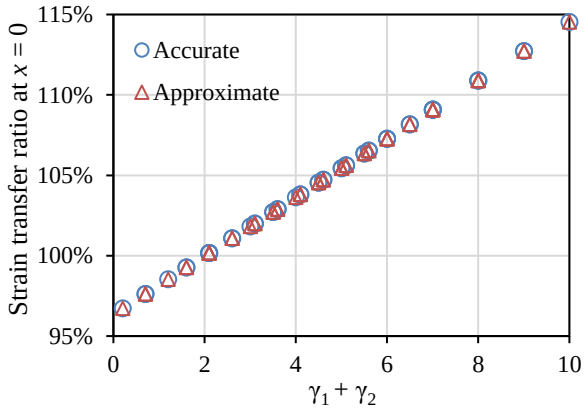

Fig. 10. Strain transfer ratio at $x = 0$. "Accurate" and "Approximate" are obtained using Eq. (42) and Eq. (44), respectively.

A brief summary of the above analysis can be made: For a non-uniform strain field, in addition to the development length at the two ends of the distributed fiber optic sensor, the strain transfer at the interface between two adjacent segments should be considered. When the segment length is no less than 0.1 m, if $(\gamma_1 + \gamma_2) < 5$, then, the effect of the strain transfer effect is less than 5%.

3.3. Experimental study

The analytical formulae of strain transfer ratio are derived for uniform and representative non-uniform strain fields, and investigated through experimentation using strain distributions measured from distributed fiber optic sensors based on Optical Frequency Domain Reflectometer (OFDR) with a sub-millimeter spatial resolution [17].

To validate the derived formulae and analysis in the above analytical study, experiments have been performed in two loading scenarios: (1) uniaxial tensile test, and (2) three-point bending test. The two tests respectively correspond to uniform strain field and non-uniform strain field with a non-differentiable point. An aluminum plate instrumented with a distributed fiber optic sensor was tested using a low-capacity load frame (load capacity: 10 kN). The strain distributions along the optical fiber were measured from the distributed sensors based on OFDR.

3.3.1. Sensing principle

The sensing principles of OFDR in optical fibers are elaborated in [19, 20]. OFDR is based on swept-wavelength homodyne interferometry. Light wave from a tunable laser source is split and sent through the measurement and reference arms of an interferometer and recombined at an optical detector. Since the two paths of light are coherent, interference fringes are generated, and related to the amplitude and phase response of the optical fiber under test. The interference fringes in frequency domain can be converted into time domain using the Fourier transform. In time domain, a map of the reflections as a function of distance along the optical fiber under test can be constructed. Hence, OFDR can be used for both spectral and time domain reflectometry, and suitable for applications that require a combination of high speed, sensitivity, and spatial resolution over intermediate length ranges (tens to hundreds of meters). The relationship between the spectral shift and the temperature/strain change is given by Eq. (56). In this study, an OFDR system (model: Luna ODisi 6) was used as the instrument and had a sub-millimeter spatial resolution and high measurement accuracy (1 με for strain, and 0.1 ℃ for temperature).

$$\Delta\nu_F = C_{\varepsilon F}\Delta\varepsilon_F + C_{TF}\Delta T_F \tag{56}$$

where $\Delta\nu_F$ is the spectral shift; $\Delta\varepsilon_F$ is the fiber strain; ΔT_F is the fiber temperature change; and $\Delta C_{\varepsilon F}$ and ΔC_{TF} are calibration constants for strain and temperature, respectively. At a constant temperature, the spectral shift is linearly related to the strain. Hence, the spectral shift can be converted into strain along the optical fiber with a calibrated strain sensitivity coefficient.

3.3.2. Tensile test

A uniaxial tensile testing of an aluminum plate instrumented with a distributed fiber optic sensor, as shown in Fig. 11(a). The aluminum plate measured 300 mm in length, 30 mm in width, and 3 mm in thickness. A distributed fiber optic sensor was attached on the surface of plate using a two-part epoxy. The fiber was connected to the distributed sensing system using the same optical fiber. The low-capacity load frame was used to apply tensile forces to the specimen. Before the tensile test, a 4-N preload was applied to allow the load frame and specimen to set. Then, the specimen was stretched to achieve 1600

με with a step size of 200 με. A clip-on strain gauge was calibrated using a caliber and used to measure the strain of the aluminum plate. The strain distribution along the optical fiber was measured at each step of loading. Fig. 11(b) shows the measured strain distributions from the distributed fiber optic sensor at different loading levels, and compares the measurement result with the analytical strain distributions. Overall, the experimental results are in good agreement with the analytical results.

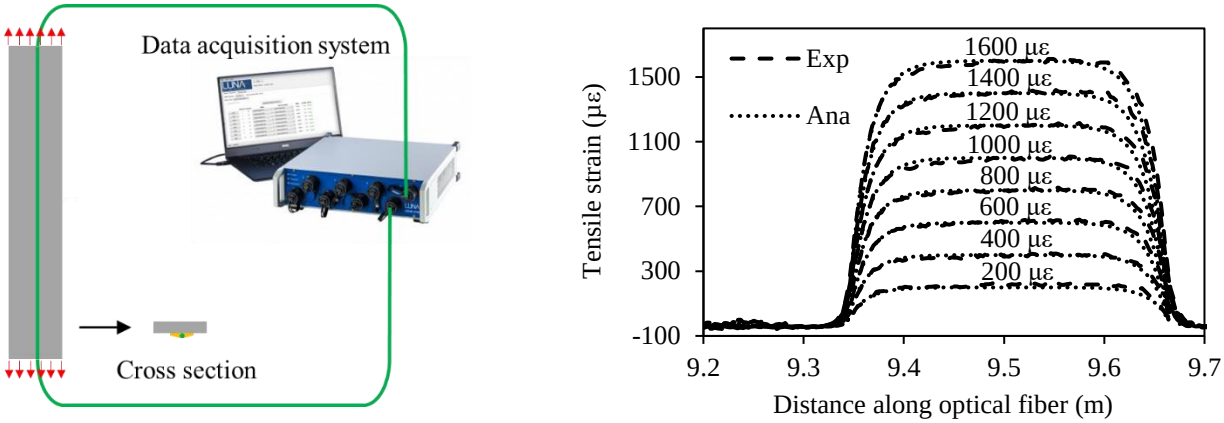

(a) (b)

Fig. 11. Uniaxial tensile test: (a) experimental setup, and (b) strain distribution results. The experimental and analytical results are represented by "Exp" and "Ana", respectively.

3.3.3. Flexural test

The same aluminum plate was tested under three-point bending using the same load frame, as depicted in Fig. 12(a). The span length was 250 mm. A 4-N preload was applied to allow the load frame and beam to set. The mid-span deflection and settlements were measured using a displacement sensor attached to the mid-span of the specimen. The mid-span deflection was changed from 0 to 1.5 mm with a step size of 0.5 mm. The strain distribution along the optical fiber was measured at each step. Fig. 12(b) compares the measured strain distributions with the analytical strain distributions. Overall, the experimental results were in good agreement with the analytical results, and thus, validated the derived formulae of strain transfer for the non-uniform strain field with a non-differentiable point.

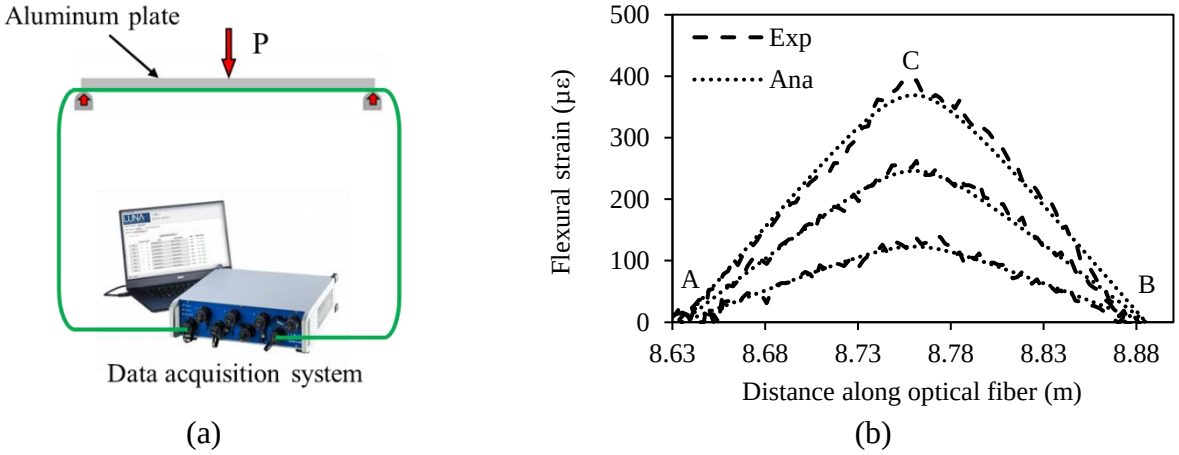

(a) (b)

Fig. 12. Bending test: (a) experimental setup, and (b) strain distribution results. The experimental and analytical results are represented by "Exp" and "Ana", respectively.

(e) Task II: Developing and Characterizing Point Fiber Optic Sensors

In Task II, we aim to develop and characterize point fiber optic sensors under deformation and corrosion. In the third quarter, three activities were performed for Task II.

The three tasks include: (1) performing an experimental study on the measurement using a representative type of point fiber optic sensor – fiber Bragg grating (FBG) sensor; (2) conducting a finite element analysis of the FBG sensor; and (3) trainings of a graduate student for theoretical analysis of fiber optic sensors.

Detailed discussion and descriptions for the following:

1. Background

Currently, there is lack of knowledge and effective technology for using point fiber optic sensors to detect, locate, and quantify interactive anomalies in pipelines. It is unclear how the point fiber optic sensors can be installed and where the sensors should be installed for improving the measurement accuracy and reliability. Therefore, there is an urgent need to develop methods to determine how the FBG sensors can be deployed to monitor anomalies accurately and reliably in pipelines.

2. Test Design

2.1. Types of anomalies

In this project, three types of anomalies are considered, including load (concentrated & distributed), vibration (noise), and corrosion (material degradation), as listed in Table 1. In the past quarter, the research focused on the effects of load and corrosion (i.e., Categories 1, 2, and 3).

Table 1. Categories of Individual and Interactive Anomalies

Category	Types of anomalies
1	Load
2	Corrosion
3	Load & Corrosion
4	Vibration
5	Vibration & Corrosion
6	Load & Vibration
7	Load & Vibration & Corrosion

2.2. Design experimental setup

The design of the experimental setup considers the anomalies in steel plates, which measure 6.75” × 6.75” × 0.125” (length × width × thickness) and have holes at the four corners of each plate. The holes measure 0.5” in diameter. The steel plates are made using A36 steel, and they are fastened to a perforated stainless-steel tabletop using nuts and bolts, as depicted in Fig. 2.1.

To mitigate corrosion of steel, the steel plates had a thin layer of epoxy costing. One FBG sensor is glued in the central axis of the steel plate using a two-part epoxy. The FBG sensor is used to monitor the condition of the steel plate.

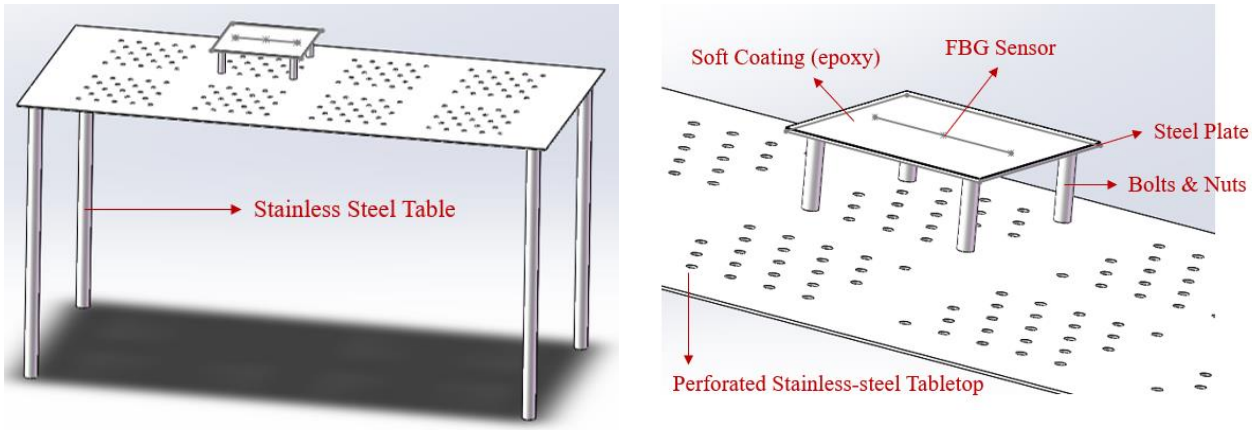

(a) (b)

Fig. 2.1. Schematic of the experimental setup: (a) overall set-up of the steel plate on the steel tabletop; and (b) elaboration of the steel plate and the FBG sensor on the plate.

For the loading test of steel plates with epoxy, a stainless-steel frame has been designed and fabricated, as shown in Fig. 2.2. The frame is made by welding a stainless-steel bar onto a stainless-steel plate. The steel bar measures 0.75” in diameter, and the steel plate measures 6” × 6” × 0.125” (length × width × thickness). After fixing the stainless-steel frame on the top surface of steel plates, mechanical loading can be applied to the steel plate of the steel frame at different levels of magnitude.

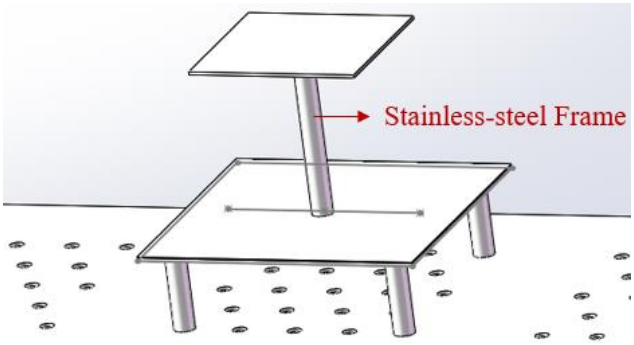

Fig. 2.2. Schematic of the loading test setup.

To simulate the realistic corrosive environment and achieve real-time monitoring of corrosion, PVC pipes with a diameter of 4” are attached on the top surface of steel plates using epoxy and filled with 3.5 wt.% sodium chloride (NaCl) solution after the adhesive is fully cured, as shown in Fig. 2.3(a). The test setup for combined loading and corrosion is shown in Fig. 2.3(b).

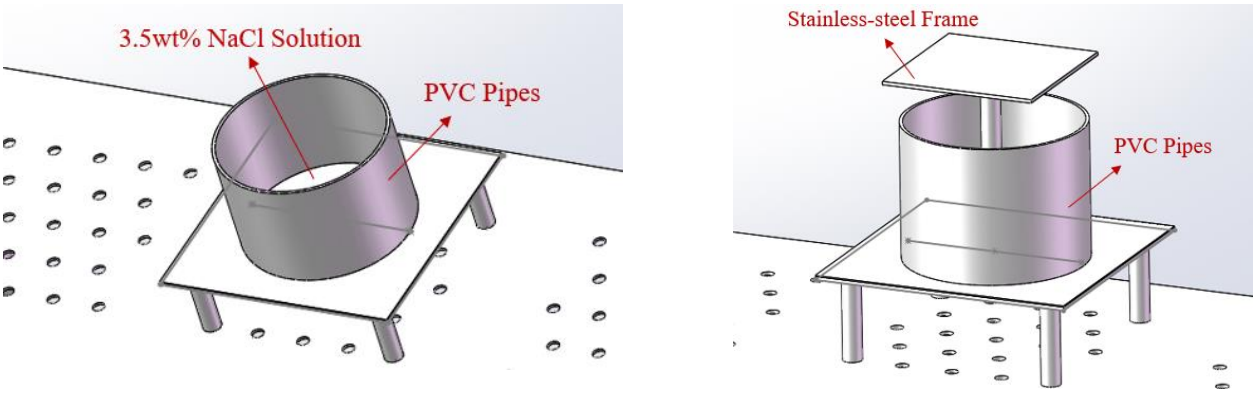

(a) (b)

Fig. 2.3. Schematic of test setup for (a) corrosion, and (b) combination of loading and corrosion.

Because the FBG sensors are point sensors, the anomalies of steel structures can only be assessed if the sensors are installed at the anomaly locations, which are unknown locations in practical application. If the anomalies do not occur exactly at the locations of the embedded sensors, or near the sensors, the effectiveness of the anomaly assessment system is questionable. Meanwhile, FBG sensors are fragile. So, using FBG sensors packaged by tubes not only can protect sensors but also can extend the sensing range of sensors, as shown in Fig. 2.4.

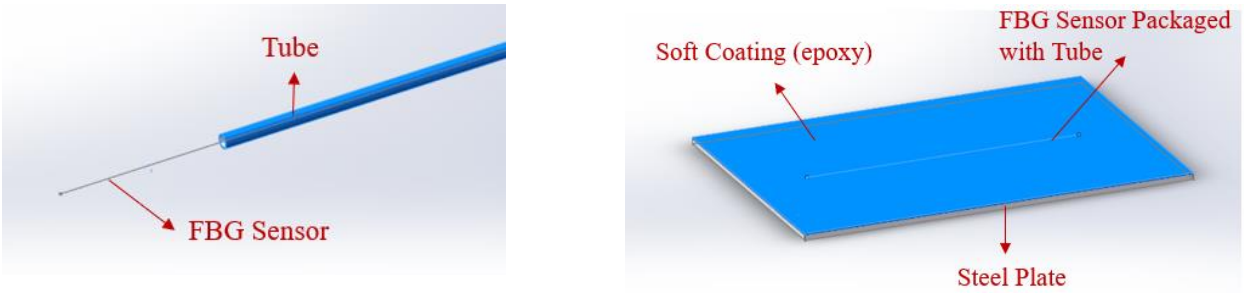

(a) (b)

Fig. 2.4. Schematic of the FBG sensor packaged with a tube.

2.3. Design tube parameters

To study the effect of tubes on the sensing of FBG sensors, FBG sensors packaged by tubes with different materials and sizes will be tested, which can be compared with bare FBG sensors. Two types of tube materials (i.e., PTFE and stainless-steel) are selected. The elastic modulus of the PTFE is similar to that of the optical fiber. Meanwhile, various diameters and wall thicknesses of selected tubes will be tested to study the size influence of tubes on sensing. The tube parameters are listed in Table 2.

Table 2. Tube parameters

Material (Model)	Size (inner diameter × outer diameter)
PTFE (SWTT-30)	$0.012'' \times 0.021''$
PTFE (STT-28)	$0.015'' \times 0.021''$
PTFE (STT-30)	$0.012'' \times 0.018''$
Stainless-steel (HTX-25T)	$0.012'' \times 0.02''$
Stainless-steel (HTX-25X)	$0.015'' \times 0.02''$
Stainless-steel (HTX-23R)	$0.012'' \times 0.025''$

2.4. Determine load value

A compression test using the MTS machine was done on a sample of a steel plate with an embedded bare FBG sensor to study the relationship between the microstrain ($\mu\varepsilon$) along the sensor and the compression load value, then determine the magnitudes of loads that need to be applied during experiments. The setup of compression test is illustrated in Fig. 2.5. Two steel plates with $1/2''$ diameter holes at the four corners were fixed with bolts and nuts. The upper steel plate was the sample with an embedded FBG sensor for compression test, and the lower steel plate was used to simulate the stainless-steel tabletop. A $1/4''$ thickness of steel plate was vertically welded to a round steel plate, and the whole was attached to the bottom of the lower steel plate to facilitate the clamping and fix the entire experimental setup by the MTS machine. The upper clamp of the MTS machine clamped a $3/4''$ diameter steel rod for applying compression load.

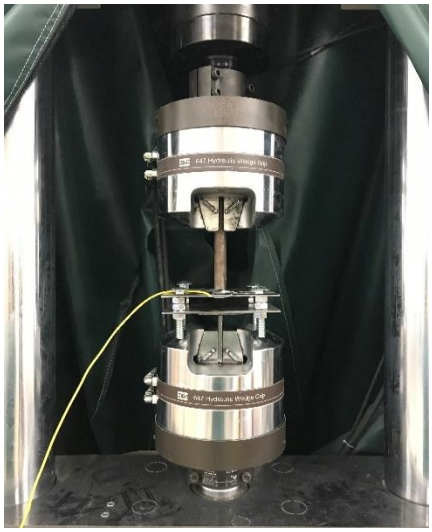

(a)

(b)

Fig. 2.5. Pictures of the compression test.

When the wavelength shifts with the increase of compression load, the change of strain along the sensor can be got as the below equation:

$$\Delta\lambda = \Delta\lambda_B - \Delta\lambda_{\text{ref}} = (1 - \mathrm{P}_e) \cdot \lambda_B \cdot \varepsilon_c \quad (1)$$

where $\Delta\lambda_B$ is Bragg wavelength change, $\Delta\lambda_{\text{ref}}$ is Bragg wavelength change of temperature reference sensor, P_e is the photo elastic constant of the fiber and ε_c is the change in strain along the sensor. During the compression test, the FBG interrogator and MTS machine were set to have the same frequency sampling (10 Hz). Therefore, the relationship between the corresponding load and strain along the sensor can be obtained.

Fig. 2.6 illustrates the teste results and it shows an approximately proportional relationship between microstrain along the sensor and axial load. Based on some experimental results of using FBG sensors to monitor the corrosion of steel plates, the jump changes in Bragg wavelength corresponding to 20 $\mu\varepsilon$ can be obviously observed both in loading tests and interactive loading and corrosion tests. So, it is determined that during the five-level loading test, each level of the load is 30 N and the five-level loads are 30 N, 60 N, 90 N, 120 N and 150 N.

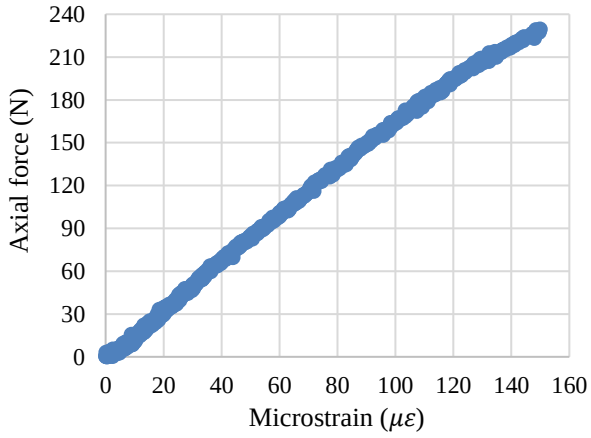

Fig. 2.6. Relationship between microstrain ($\mu\varepsilon$) and axial load (N).

2.5. Determine tube length

Based on the compression test results of the sample with embedded bare FBG sensor, after a five-level loading process, theoretically, the sensor will produce 100 $\mu\varepsilon$ in the longitudinal direction. Therefore, when carrying out the loading test on the sample with an embedded FBG sensor packaged by a tube, it should be guaranteed that at least 120 $\mu\varepsilon$ can be detected within the tube length. A numerical plate model using ANSYS was built with the dimension of $6.75'' \times 6.75'' \times 0.125''$. The selected material is structural steel and the soft coating (epoxy) is ignored because epoxy has a relatively small stiffness compared to steel. The plate model has fixed supports at four corner points and a five-level load was applied on a circle of $3/4''$ diameter at the center of the plate step by step.

In the analysis results, a strain cloud diagram along the X-axis direction, i.e., the longitudinal direction of the sensor, is displayed, the green range corresponding to the range of 20 $\mu\varepsilon$ to 120 $\mu\varepsilon$, as shown in Fig. 2.7. There is no green range in Fig. 2.7(a), because the maximum strain on the front side of the steel plate did not exceed 20 $\mu\varepsilon$ after the first-level load (30N) was applied, which was not in the green setting range. Based on Fig. 2.7(e), the maximum green range along the X-axis direction is about 60% of the steel plate side length that is $6.75''$, so the tube length is determined as $4''$ ($60\% \times 6.75'' = 4.05'' \approx 4''$).

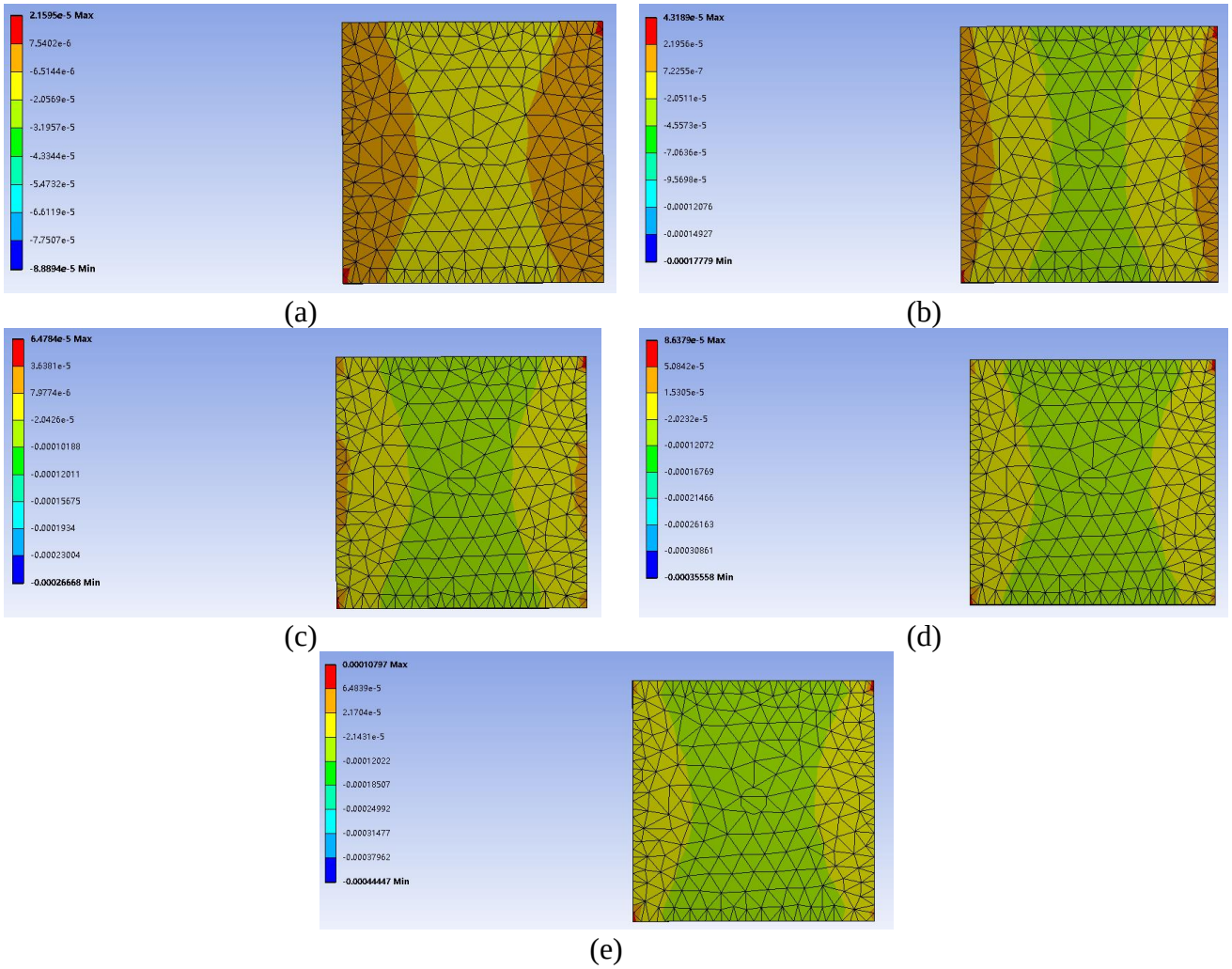

Fig. 2.7. Strain cloud diagram along the X-axis direction of five-level load: (a) 30 N, (b) 60 N, (c) 90 N, (d) 120 N, and (e) 150 N.

2.6. Theoretical analysis of FBG sensor packaged with tube

Assume that the FBG sensor packaged with the tube is a simply supported beam subjected a concentrated force at the center or a symmetrical uniform load, as shown in Fig. 2.8. The bottom of the tube is adhered to the steel plate. When a force is applied, the top surface of the tube will be deformed, and the cross sections of the tube ends will rotate around the two points A and B, and generate strains in the FBG sensor, resulting in wavelength shifts. Because the FBG sensor cannot distinguish the concentrated and the distributed force, the distributed force can be converted into a concentrated force acting at the midpoint of the tube, which can use the same theoretical Equations (2) to (5).

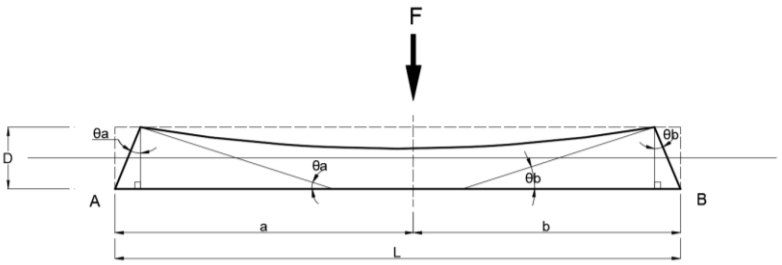

(a)

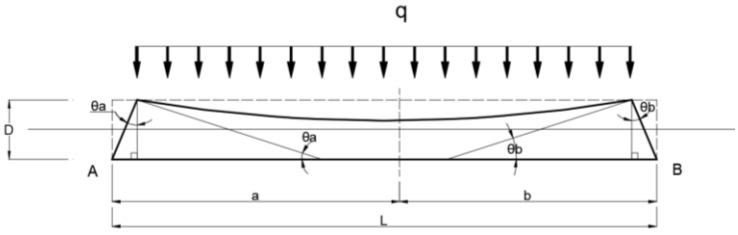

(b)

Fig. 2.8. Diagram of the simple-supported beam model: (a) Diagram of concentrated force; and (b) Diagram of distributed force.

The theoretical calculation process of this simple-supported beam model under concentrated load is as follows:

$$\theta_A = \frac{Fb(L^2 - b^2)}{6LEI}, \quad \theta_B = -\frac{Fab(L + a)}{6LEI} \tag{2}$$

where θ_A and θ_B are rotation angels at the cross sections of both ends of the tube (clockwise rotation is positive and counterclockwise rotation is negative), F is the concentrated force, L is the length of the tube ($4''$), a and b are the lengths from concentrated force to cross sections at both ends, E is the Elastic Modulus of tube and I is the Moment of Inertia.

$$\Delta L_A = tan\theta_A \cdot D, \quad \Delta L_B = tan\theta_B \cdot D \tag{3}$$

where ΔL_A and ΔL_B are the displacements of the tube upper surface at the two end points and D is the outer diameter of the tube.

$$\Delta L = \frac{1}{2}(\Delta L_A + \Delta L_B) = \frac{1}{2}(tan\theta_A + tan\theta_B) \cdot D \tag{4}$$

where ΔL is the displacement of the FBG sensor.

$$\varepsilon_c = \Delta L / L \tag{5}$$

where ε_c is the strain generated in the FBG sensor. Combining Equation (1) and (5) can achieve the wavelength shift of the FBG sensor when the concentrated force is applied.

3. Experimental Test Process

3.1. Calibration test

Fig. 2.9 shows the calibration of the strain sensitivity of the FBG sensor. A steel plate was instrumented with an FBG sensor and stretched using an MTS load frame. The elongation of the steel plate and the shift of Bragg wavelength were measured by the load frame and sensor interrogator, respectively. The load frame and sensor interrogator have the same sampling frequency (10 Hz), and they were synchronized.

(a) (b)

Fig. 2.9. Pictures of tension test.

According to the obtained axial deformation, the overall axial strain of the steel plate can be calculated as the following equation:

$$\varepsilon_1 = \frac{\Delta l}{l} \tag{6}$$

where ε_1 is the strain of the steel plate; Δl is the elongation; and l is the length of the steel plate.

Meanwhile, based on the Bragg wavelength shift from the sensor interrogator and Equation (6), the strain (ε_2) in the sensor can be calculated. Fig. 2.10 shows the relationship between ε_1 and ε_2 under different conditions. In the subsequent experiments, the actual strain in the steel plate can be calculated based on the relationship obtained by sensor calibration.

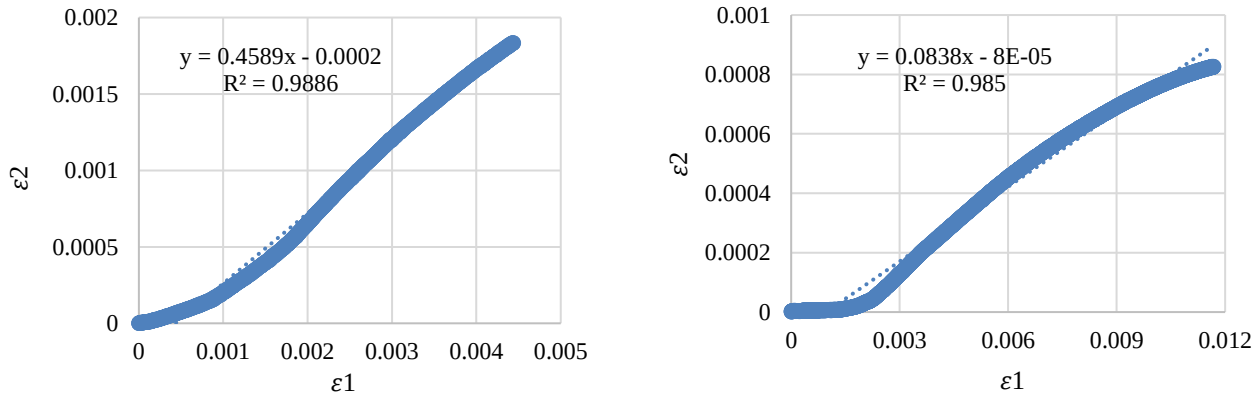

(a) (b)

Fig. 2.10. Tension test results of steel plates: (a) steel plate with a bare FBG; and (b) steel plate with an FBG packaged by PTFE tube.

3.2. Loading test

3.2.1. Loading test of bare FBG

When preparing the tests, the steel plates should be wiped with alcohol and performed rust removal treatment first, in order to avoid the differences of steel plates, which will affect the subsequent test results. Then, found the central axis of the steel plate and marked it with a marker. Straightened and glued the FBG sensor to the position of the central axis. FBG sensors are point optic fiber sensors, therefore, it should be ensured that the sensing area (Bragg gratings) of the sensor was at the center of the central axis. In this step, 502 glue was used, because it can quickly dry and glue the sensor in 5 minutes for making the next soft coating. After the steel plates were coated with soft coating (epoxy), they should be left for at least 24 hours for the coating to completely cure before the loading tests can be performed.

After the coating was cured, bolts and nuts were used to fix steel plates on the stainless-steel table. To ensure that there was a distance between the table and the steel plates, two nuts at each corner were used, which can ensure that the four bolt legs did not deform during loading. At the beginning of the loading test, the tape was used to secure the stainless-steel frame on the central point of the steel plate. Then, based on the designed five-level load values (30N, 60N, 90N, 120N, 150N), 10 stainless-steel plates were made and placed 2 stainless-steel plates at each stage of loading. A total of 4 samples with embedded bare FBG sensors in epoxy were made, one of which was a temperature-compensated sample, numbered B1, B2, B3, and BT4, as shown in Fig. 2.11. For each test, one test sample and the temperature-compensated sample were connected to the interrogator at the same time. A five-level loading and unloading cycle was performed for each loading test and each sample was loaded and unloaded three times. In order to make the sensor interrogator completely respond to the Bragg wavelength shift, the interval of load application was 2 minutes.

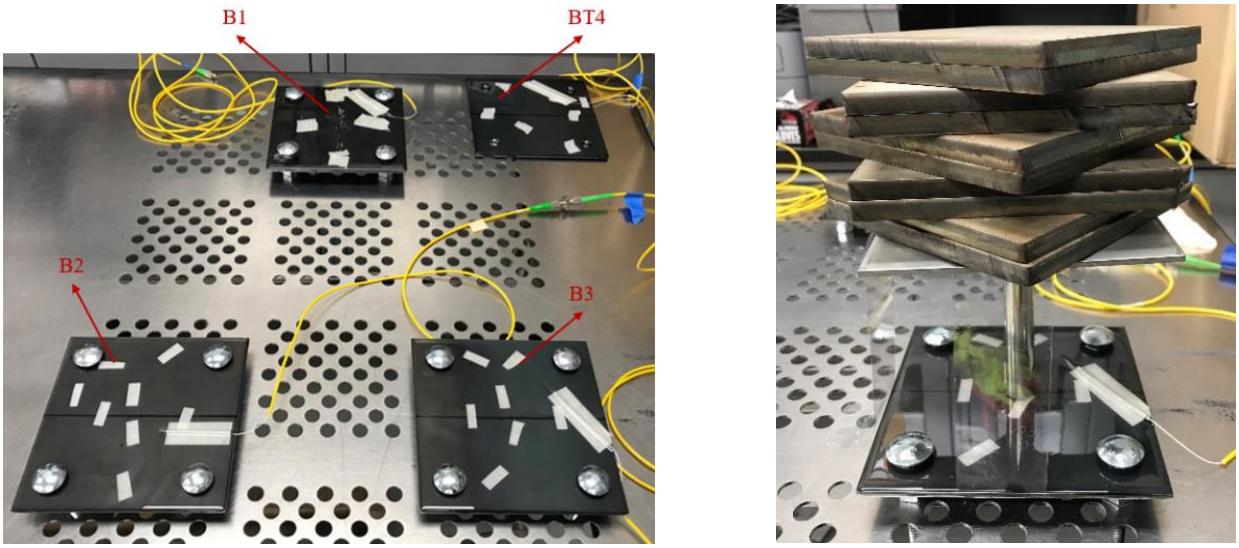

(a) (b)

Fig. 2.11. Experimental setup of loading test.

Fig. 2.12 shows the loading test results about the relationship between time and produced microstrain of steel plates with bare FBG sensors. There are differences in Bragg wavelength shifts between the different specimens (B1, B2, and B3). In particular, the results from B1 are different from the results from B2 and B3. The reason is that when bare FBG sensors were glued, B2 and B3 were completely fixed. Therefore, the FBG sensors of B2 and B3 were deformed and bent during the epoxy

curing process, which resulted in larger Bragg wavelength shifts during tests. So, the test results of B1 are more reliable. The results of B1 are also consistent with the results of previous compression test. After the five-level loading, the sensor produced a total of approximately 100 $\mu\varepsilon$. The changes of Bragg wavelength shift with time are illustrated in Fig. 2.12. The obvious step changes in the loading and unloading of the Bragg wavelength at each stage indicates that specimen can also perform significant changes in Bragg wavelength when subjected to loads during the combined loading and corrosion tests.

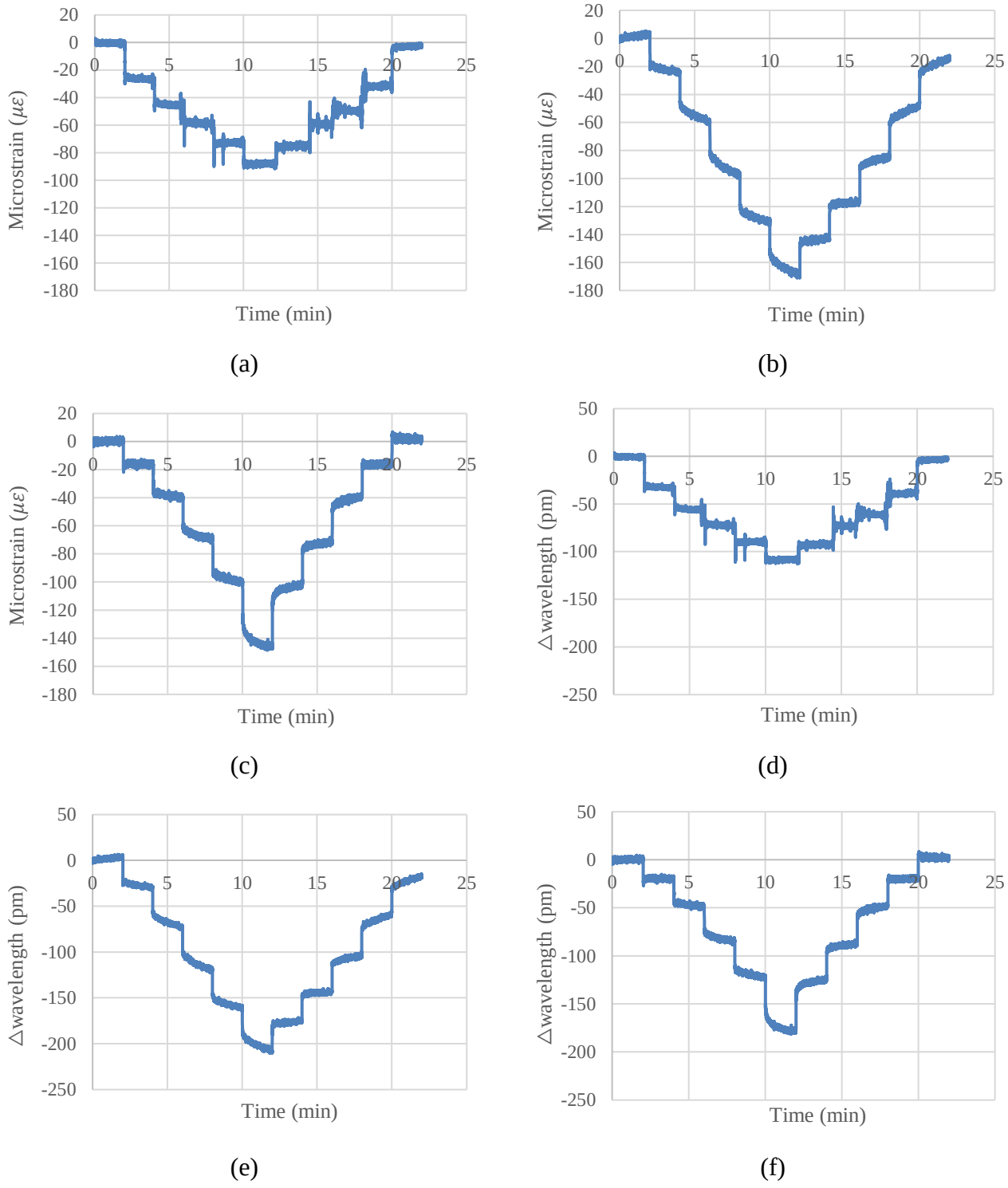

Fig. 2.12. Loading test results of steel plates with bare FBG sensors: (a) strain in B1, (b) strain in B2, (b) strain in B3, (b) wavelength in B1, (b) wavelength in B2, and (b) wavelength in B3.

3.2.2. Loading test of FBG with PTFE tube (SWTT-30)

The preparation of experimental samples was similar to that of the samples with bare FBG sensors, but the FBG sensors were needed to be packaged with PTFE tubes (SWTT-30). First, inserted the FBG sensor into a 4″ PTFE tube. Then, straightened the sensing area of the sensor, attached it on a ruler with tape and marked the center point of its sensing area with a marker so that this point corresponded to the center point of the tube. After fixing the position of the tube, glue was used to fix the two ends of the tube with the sensor. The completed samples are shown in Fig. 2.13, and they are numbered as S30-1, S30-2, S30-3, and ST30-4.

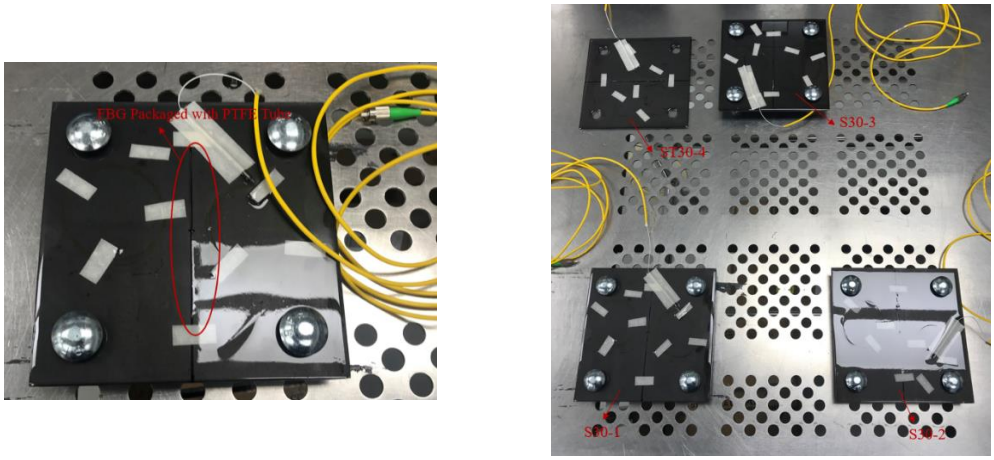

(a) (b)

Fig. 2.13. Steel plates of FBG packaged with PTFE tube.

(f) Task IV: Student Training and Reporting

In Task IV, we have been training two graduate students (one from Stevens and one from NDSU) and two undergraduate students. Through the research, the students are trained, aiming to become future experts in the related fields.

In the third quarter, two activities were performed for Task IV, including (1) training two graduate students and two undergraduate researchers to conduct laboratory testing of the distributed fiber optic sensors and point fiber optic sensors; and (2) an outreach event named “Smart Infrastructure” to primary school students as a part of the Sustainable Challenge Program in Jersey City.

2.4 Student Mentoring

During the second quarter, two graduate students (Xiao Tan, Ph.D. student from Stevens, and Luyang Xu, Ph.D. student from NDSU) and two undergraduate research assistants (Gina Blazanin and Hashem Sonbol) were trained to work on this project.

The two graduate students were trained to conduct laboratory testing and finite element analysis for the distributed fiber optic sensors and point fiber optic sensors. Two undergraduate research assistants assisted the graduate students to carry out the finite element analysis.

2.5 Outreach Activities

On May 29th, 2020 (9:00 am to 11:30 pm), an outreach event named “Smart Infrastructure” workshop was conducted based on this project. The workshop is a part of the Sustainable Challenge Program in New Jersey. The PI Bao serves on the panel of the Program. This workshop intended to let

the primary school students have basic knowledge to plan and build smart pipelines. It is expected to encourage and generate interests for young kids to pursue pipeline engineering for future college education or careers. Table 3 is the schedule of the event.

Table 3. Outreach Workshop Schedule

9:00	-	9:15	Introduction of the workshop and sustainable challenge program
9:15	-	11:15	Presentations and discussions
11:15	-	11:30	Concluding remarks and plans

More than 10 primary school students attended this workshop. One graduate student volunteered in this outreach event to coach the primary school students. Fig. 3.1 shows a screenshot of the virtual meeting with students.

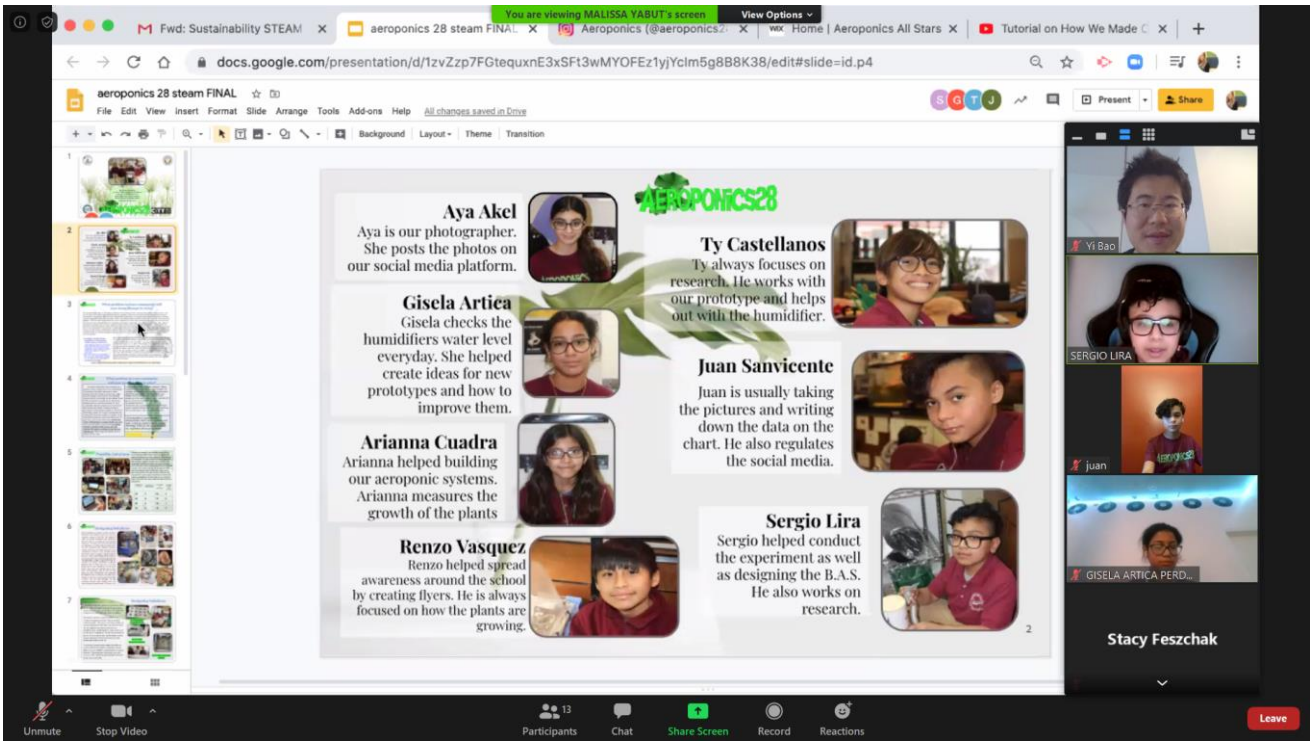

Fig. 11. Virtual meeting with primary school students in Jersey City.

3. Future work

In the fourth quarter, there will be four objectives:

1) Focus on the remaining activities planned in Task I: Developing and Characterizing Distributed Fiber Optic Sensors. Based on the laboratory testing of the distributed fiber optic sensors, we will conduct further experiments and theoretical studies on using the optical fiber as distributed sensors to test the sensor responses under multiple individual types of defects and the combined defect conditions.

2) Conduct the research activities planned in Task II: Distinguishing Interactive Anomalies Using Point Fiber Optic Sensors. More specifically, fiber Bragg grating sensors will be tested to evaluate the performance of point sensors under multiple individual types of defects and the combined defect conditions.

3) Supervise the two graduate students in performing research Tasks I and II. The two graduate students will conduct the experiments and analyze the data under the supervision of the PI Bao and the Co-PI Huang.

4) Conduct an “Intelligent Pipeline” workshop outreach event in the Jersey City Sustainable Challenge Program to K-12 students in Jersey City. Dr. Yi Bao and a graduate student will hold a virtual meeting with local primary school students. In the virtual meeting, we will present the research progress and chat with the students.

References

[1] Huang, Y., Bao, Y., Chen, G. and Zhou, Z., (2019). “A constrained cylinder model of strain transfer for packaged fiber Bragg grating sensors embedded in inelastic medium.” Structural Control and Health Monitoring, 26(5), p.e2335.

[2] Bao, Y., 2017. Novel applications of pulse pre-pump Brillouin optical time domain analysis for behavior evaluation of structures under thermal and mechanical loading. Ph.D. Dissertation, Missouri University of Science and Technology.

[3] [3] Pak, Y. E. (1992). "Longitudinal shear transfer in fiber optic sensors." Smart Materials and Structures, 1(1), 57.

[4] Sirkis, J. S., and Haslach Jr, H. W. (1991). "Complete phase-strain model for structurally embedded interferometric optical fiber sensors." Journal of Intelligent Material Systems and Structures, 2(1), 3-24.

[5] Cox, H. (1952). "The elasticity and strength of paper and other fibrous materials." British Journal of Applied Physics, 3(3), 72.

[6] Ansari, F., and Libo, Y. (1998). "Mechanics of bond and interface shear transfer in optical fiber sensors." Journal of Engineering Mechanics, 124(4), 385-394.

[7] Duck, G., and LeBlanc, M. (2000). "Arbitrary strain transfer from a host to an embedded fiber-optic sensor." Smart Materials and Structures, 9(4), 492.

[8] Li, Q., Li, G., Wang, G., Ansari, F., and Liu, Q. (2002). "Elasto-plastic bonding of embedded optical fiber sensors in concrete." Journal of Engineering Mechanics, 128(4), 471-478.

[9] Li, D.-S., Li, H., Ren, L., and Song, G. (2006). "Strain transferring analysis of fiber Bragg grating sensors." Optical Engineering, 45(2), 024402.

[10] Zhou, Z., Li, J., and Ou, J. (2007). "Interface transferring mechanism and error modification of embedded FBG strain sensors." Frontiers of Electrical and Electronic Engineering in China, 2(1), 92-98.

[11] Li, H.-N., Zhou, G.-D., Liang, R., and Li, D.-S. (2007). "Strain transfer analysis of embedded fiber Bragg grating sensor under nonaxial stress." Optical Engineering, 46(5), 054402.

[12] Ling, H.-Y., Lau, K.-T., Cheng, L., and Chow, K.-W. (2005). "Embedded fibre Bragg grating sensors for non-uniform strain sensing in composite structures." Measurement Science and Technology, 16(12), 2415.

[13] Li, H.-N., Zhou, G.-D., Ren, L., and Li, D.-S. (2009). "Strain transfer coefficient analyses for embedded fiber Bragg grating sensors in different host materials." Journal of Engineering Mechanics, 135(12), 1343-1353.

[14] Jiang, Z., Lian, J., Yang, D., and Dong, S. (1998). "An analytical study of the influence of thermal residual stresses on the elastic and yield behaviors of short fiber-reinforced metal matrix composites." Materials Science and Engineering: A, 248(1-2), 256-275.

[15] Bao, Y., Meng, W., Chen, Y., Chen, G., and Khayat, K. H. (2015). "Measuring mortar shrinkage and cracking by pulse pre-pump Brillouin optical time domain analysis with a single optical fiber." Materials Letters, 145, 344-346.

[16] Bao, Y., and Chen, G. (2015). "Strain distribution and crack detection in thin unbonded concrete pavement overlays with fully distributed fiber optic sensors." Optical Engineering, 55(1), 011008.